Catalysis Letters (2022) 152:872–882
https://doi.org/10.1007/s10562-021-03677-7

Enhanced Low-Temperature Activity of CO_2 Methanation Over Ni/CeO_2 Catalyst

Yuan Ma[1,2] · Jiao Liu[1] · Mo Chu[3] · Junrong Yue[1] · Yanbin Cui[1] · Guangwen Xu[1,4]

Received: 9 February 2021 / Accepted: 24 May 2021 / Published online: 28 May 2021

Abstract

CeO_2 nanorods (CeO_2-nrs), CeO_2 nanocubes (CeO_2-ncs) and CeO_2 nanopolyhedrons (CeO_2-nps) were prepared by hydrothermal method and then NiO crystallites were deposited on these supports by precipitation-deposition, respectively. The physicchemical properties of Ni/CeO_2 catalysts were characterized and performances for carbon dioxide methanation reaction were tested. The Ni/CeO_2-nrs sample shows well metal dispersion and high concentration of oxygen vacancy, which leads to the high catalytic activity for CO_2 methanation. Especially at 300 °C, the CO_2 conversion could reach 60%. Further analysis reveals that the content of oxygen vacancy has a positive correlation with the surface area of catalyst. The largest surface area results in the most of oxygen vacancy on the Ni/CeO_2-nrs catalyst, and then a large amount of CO_2 could be activated at low temperatures. Meanwhile, large surface area facilitates the dispersion of active metals, and improves the degree of H_2 activation. The combined effect results in the promotion of catalytic activity for CO_2 methanation at low temperatures.

Graphic Abstract

CeO_2 nanorods (CeO_2-nrs), CeO_2 nanocubes (CeO_2-ncs) and CeO_2 nanopolyhedrons (CeO_2-nps) supported Ni catalysts were prepared. These catalysts ware tested for CO_2 methanation and further characterized by BET, XPS, TEM, H_2-TPR and TPD. The results showed that the content of oxygen vacancy has positive correlation with the specific surface area of catalyst.

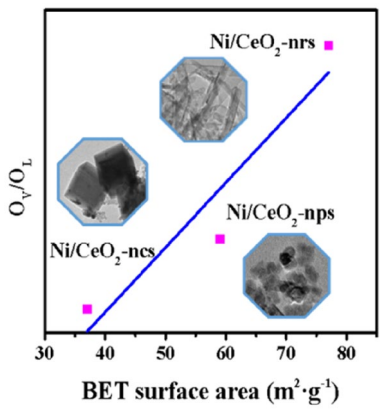

Keywords Carbon dioxide · Methane · CeO_2 · Catalyst · Support · Oxygen vacancy · Ni

✉ Jiao Liu
liujiao@ipe.ac.cn

[1] State Key Laboratory of Multi-Phase Complex Systems, Institute of Process Engineering, Chinese Academy of Sciences, Beijing 100190, China

[2] Ordos Environmental Protection Investment Co., Ltd., Ordos 017010, Inner Mongolia, China

[3] School of Chemical and Environmental Engineering, China University of Mining and Technology (Beijing), Beijing 100083, China

[4] Institute of Industrial Chemistry and Energy Technology, Shenyang University of Chemical Technology, Shenyang 110142, Liaoning, China

1 Introduction

Carbon dioxide as an important component of greenhouse gas and C1 resource has been widely investigated for its capture, storage and utilization [1–3]. CO_2 methanation (known as Sabatier reaction) which would reduce CO_2 emissions and produce natural gas, is considered to be one of the most effective and practical technologies for CO_2 recycling [4–6]. As an exothermic reaction, CO_2 methanation is favored at low temperatures. However, inert CO_2 shows a slow conversion rate at temperatures < 350 °C due to the kinetic limitation. Therefore, active catalyst is necessary to reduce the activation energy for CO_2 methanation [7].

Noble metals such as Ru and Rh present high activity and selectivity for low-temperature CO_2 methanation, but Ni-based catalysts are more commonly used due to their high activity and low cost [8]. Al_2O_3, ZrO_2, SiO_2, CeO_2 and many other oxides have been exploited as supports for Ni catalysts in CO_2 methanation. Sun et al. [9–11] prepared a nickel catalyst supported on nanosheet γ-Al_2O_3 and the results indicated that the well dispersed Ni crystallites with small diameter and moderate basic sites on support resulted in a good catalytic activity for CO_2 methanation. In addition, this catalyst exhibited well stability at 325 °C during 40 h time-on-stream. Tada et al. [12] studied the CO_2 methanation over the Ni-based catalysts with different supports (i.e., CeO_2, α-Al_2O_3, TiO_2, and MgO) and found that Ni/CeO_2 catalyst showed high CO_2 conversion, especially at temperatures lower than 400 °C.

The catalytic activity is highly correlated with the reaction mechanism (e.g., the reaction intermediate and route) and different catalysts may show different mechanisms [13, 14]. Pan et al. [15] compared the CO_2 methanation over Ni/Al_2O_3 and Ni/$Ce_{0.5}Zr_{0.5}O_2$ catalysts. The results revealed that CO_2 adsorbed on medium basic sites in Ni/$Ce_{0.5}Zr_{0.5}O_2$ catalyst and formed monodentate carbonates while CO_2 adsorbed on strong basic sites in Ni/γ-Al_2O_3 will not participate in the reaction. Monodentate formate derived from monodentate carbonate on medium basic sites could be hydrogenated more quickly than bidentate formate derived from hydrogen carbonate which resulted in higher activity of Ni/$Ce_{0.5}Zr_{0.5}O_2$ than Ni/γ-Al_2O_3. The oxygen vacancies also affect the formation of intermediate products and further influence the catalyst activity in the CO_2 methanation. Jia et al. [16] found that the plasma decomposition caused the formation of Ni-ZrO_2 interficial sites with more oxygen vacancies, which played crucial roles in CO_2 activation and methanation. Wang et al. [17] compared the CO_2 methanation mechanisms over Ru/CeO_2 and Ru/α-Al_2O_3 catalysts, respectively. It was revealed that CO_2 methanation underwent formate route over Ru/CeO_2 catalyst, and the formate dissociation to methanol catalyzed by oxygen vacancy was the rate-determining step. In contrast, CO_2 methanation underwent CO route over Ru surface in Ru/α-Al_2O_3 with the absence of oxygen vacancy, demonstrating active site dependent catalytic mechanism toward CO_2 methanation. In addition, the catalytic activity evaluation and the oscillating reaction over Ru/CeO_2 catalyst further proved that the oxygen vacancy catalyzed the rate-determining step with a much lower activation temperature compared with Ru surface in Ru/α-Al_2O_3 (125 versus 250 °C).

High oxygen storage capacity (OSC) coupled with a high oxygen transport capacity gives CeO_2 a unique property for catalyst applications. Previous studies showed that the OSC of CeO_2 was related to its exposed crystal planes. Oxygen storage takes place both at the surface and in the bulk as {110}/{100} planes exposed while the storage restricted at the surface as {111} planes exposed [18]. It has been reported that CeO_2-supported metal catalysts (i.e., Ru, Ni et al.) were active for CO_2 methanation, particularly at low temperatures. Sakpal [19] investigated the catalytic activity of Ru-CeO_2 catalysts with different morphologies and found that the Ru/CeO_2/r catalyst (CeO_2/r = CeO_2 rods) was easier to be reduced and contained more oxygen vacancies compared to Ru/CeO_2/o and Ru/CeO_2/c catalyst (CeO_2/o = CeO_2 octahedra, CeO_2/c = CeO_2 cubes). Characterization further revealed that the highest concentration of oxygen vacancies led to the most active catalyst and the adsorption of CO_2 at an oxygen vacancy was the rate-determining step. A Ni catalyst supported on ceria nanorods was also compared with the Ni/CeO_2 commercial products and state-of-the-art literature catalysts for CO_2 methanation [20]. The high efficiency of the former catalyst was presumed to be the formation of highly active interfacial sites with abundance in Ce^{3+} for a low-temperature methanation process. Zhou et al. [21] prepared a Ni/CeO_2 catalyst by the hard-template method and the catalytic properties were also investigated by CO_2 methanation. In-situ FT-IR and in-situ XPS results indicated that CO_2 molecules could be reduced by active metal Ni species and surface oxygen vacancies to generate active CO species and then promoted CO_2 methanation. The CO_2 conversion and CH_4 selectivity reached 91.1% and 100% at 340 °C and atmospheric pressure.

To date, the majority of studies have shown the oxygen vacancy could promote CO_2 methanation. However, few studies focus on the factors affecting the concentration of oxygen vacancy on the catalyst. Thus, this work prepared CeO_2 with different morphologies, such as nanorods, nanocubes, and nanopolyhedrons (denoted as CeO_2-nrs, CeO_2-ncs, and CeO_2-nps, respectively) as supports that dominantly expose {110}, {100}, and {111} planes, respectively. Subsequently, Ni-supported catalysts were prepared by precipitation–deposition, and applied in the CO_2 methanation.

The relationship between the physical and chemical structures of the catalysts and their catalytic performances are analyzed and then the main factors affecting the catalytic activities of Ni/CeO_2 catalysts with different morphologies in the CO_2 methanation are explored.

2 Experimental

2.1 Catalyst Preparation

The CeO_2 supports with different morphologies were synthesized via a previously reported hydrothermal method [19]. NaOH (96.0 g) and $Ce(NO_3)_3{\cdot}6H_2O$ (8.68 g) were dissolved in deionized water (350 and 50 mL) respectively. The two solutions were then mixed and stirred for 30 min, after which the resulting mixture was transferred to a 100 mL Teflon-lined stainless-steel autoclave, and hydrothermally treated at 180 °C for 24 h. The precipitate was then collected by filtration, and thoroughly washed with distilled water and ethanol. CeO_2-ncs was obtained by drying at 60 °C for 10 h and subsequently calcined at 500 °C for 4 h. The synthesis of CeO_2-nrs and CeO_2-nps were carried out also with the above procedures, with the exception that a hydrothermal temperature of 100 °C was employed for CeO_2-nrs, while for CeO_2-nps, 0.16 g of NaOH was used.

The Ni/CeO_2 catalysts were then prepared via a precipitation-deposition method. An aqueous solution of $Ni(NO_3)_2{\cdot}6H_2O$ was mixed with the support at 60 °C over 2 h (the theoretical nickel loading is 20 wt.%). The pH was adjusted to 10 with a 1 $mol{\cdot}L^{-1}$ NaOH aqueous solution, and the suspension was further stirred and aged at 60 °C for 10 h. The precipitate was then collected by filtration, thoroughly washed with distilled water, dried at 60 °C for 12 h, and calcined at 500 °C for 4 h. Finally, the calcined catalyst was ground and screened to 180–425 μm prior to evaluation of the catalytic activity.

2.2 Catalyst Characterization and Analysis

N_2 adsorption–desorption isotherms at − 196 °C were obtained on a Micrometrics ASAP 2020 HD88 analyzer. Before measurement, the samples were degassed under vacuum at 200 °C for 12 h. The crystal structure of the prepared catalysts was analyzed with X-ray power diffractometry (XRD, X'Pert MPD Pro, PANalytical) at its Cu K_α radiation of $\lambda = 0.154$ nm. The patterns were recorded with a scan angle range 10°–90° at a scanning speed of 8° min^{-1}. The Ni loading on the supports was determined by X-ray fluorescence (XRF, AXIOX, PANalytical). Transmission electron microscopy (TEM) and high-resolution TEM (HRTEM) images were obtained on a JEOL JEM-2100 electron microscope operated at an acceleration voltage of 200 kV.

The temperature programmed reduction (TPR) and temperature programmed desorption (TPD) properties of the catalysts were determined using an Auto Chem II2920 instruments (Micrometrics) coupled with a mass spectrometer (MS, TILON, US). Prior to the measurements, the sample (~ 0.1 g) was heated from room temperature to 200 °C at a rate of 10 °C min^{-1}, and then maintained for 1 h under a flow of He. After cooling the sample to 50 °C, the H_2-TPR profile was recorded by increasing the temperature to 900 °C at a rate of 10 °C min^{-1} under a binary gas flow (10 vol.% H_2/Ar). Prior to the CO_2-TPD test, the catalyst (~ 0.1 g) was initially reduced in situ under a flow of H_2/Ar at 600 °C for 2 h, and then cooled to 50 °C under an Ar atmosphere. The sample was then saturated with 10 vol.% CO_2/Ar for 1 h and heated to 900 °C at a rate of 10 °C min^{-1} under a flow of He. The desorbed CO_2 was detected simultaneously using a thermal conductivity detector (TCD) and by MS. For the H_2-TPD measurements, the reduced sample (~ 0.1 g) was subjected to an atmosphere of 10 vol.% H_2/He at 50 °C for 2 h prior to performing the measurements in a flow of He upon heating from 50 to 900 °C at a rate of 10 °C min^{-1}. The hydrogen consumption was calculated based on the area of the hydrogen desorption peak. The Ni dispersion (D) and particle size (d_{Ni}) were calculated as follows:

$$D(\%) = \frac{Y \times M}{W} \times F_s \times 100\% \tag{1}$$

$$d_{Ni} = \frac{6 \times 10^3 \times W}{Y \times \sigma_{Ni} \times F_S \times \rho_{Ni}} \tag{2}$$

where Y denotes the H_2 adsorption capacity (mol g^{-1}), M is the molecular weight of Ni (58.69 g mol^{-1}), W is the Ni loading on the support (%), $F_S$is the stoichiometric factor (H_2/Ni = 1/2), σ_{Ni} is the atomic cross-sectional area of Ni (0.0649 nm^2), and ρ_{Ni} is the density of Ni metal (8.902 g cm^{-3}).

The X-ray photoelectron spectroscopy analysis was performed using an AXIS Ultra XPS spectrometer running at 15 kV and 15 mA with monochromomator Al Kα radiation ($h\nu = 1486.7$ eV). The binding energy (BE) values were related to the C 1s peak of contaminant carbon at 286.8 eV with an uncertainty of ± 0.2 eV. The obtained spectra were fitted using Gaussian–Lorentzian curves to more accurately extract the binding energies of the different element core levels.

2.3 Evaluation of the Catalytic Activity

The activity of the catalyst was evaluated at atmospheric pressure in a quartz fixed-bed reactor with an inner diameter of 16 mm. Before reaction, the catalyst (500 mg) was reduced under a stream of 10 vol.% H_2/N_2 (50 mL min^{-1}) at 600 °C over 4 h. Then, the reactor was cooled down to reaction

temperature under N_2 flow (50 mL min^{-1}), and a mixture gas of $H_2/N_2/CO_2$ with volume ratio of 4/1/1 was introduced into the reactor and the gas hourly space velocity (GHSV) was 36,000 h^{-1}. The reaction temperature was monitored by a thermocouple close to the bottom of the catalyst bed. The product composition was analyzed with a micro gas chromatograph (Micro3000, Agilent) equipped with TCD. The flow rates of H_2, N_2, and CO_2 were controlled by mass flow meters, and N_2 was used as an internal standard to calculate the volume flow of each component in the product. The CO_2 conversion (X_{CO2}) and CH_4 selectivity (S_{CH4}) were calculated with the following equations:

$$X_{CO_2} = \frac{f_{in}y_{CO_2,in} - f_{out}y_{CO_2,out}}{f_{in}y_{CO_2,in}} \times 100\% \quad (3)$$

Table 1 Physic-chemical properties of Ni/CeO_2 catalysts

Catalyst	BET surface area [a] (m^2 g^{-1})	Ni loading [b] (wt.%)	D (%) [c]	d_{Ni} (nm) [c]
Ni/CeO_2-nrs	76.6	18.75	10.43	11.2
Ni/CeO_2-nps	58.4	19.27	2.96	39.5
Ni/CeO_2-ncs	36.1	20.44	2.26	51.7

[a]Calculated with BET equation

[b]Determined by XRF measurement

[c]Calculated from H_2-TPD profiles

$$S_{CH_4} = \frac{f_{out}y_{CH_4,out}}{f_{in}y_{CO_2,in} - f_{out}y_{CO_2,out}} \times 100\% \quad (4)$$

where the X_{CO2} and S_{CH4} is the CO_2 conversion and CH_4 selectivity; f_{in} and f_{out} is the molar feed rate of the import and export flow in the reactor; $y_{CO2,in}$, $y_{CO2,out}$, and $y_{CH4,out}$ is the volume fraction of the import and export of CO_2 and CH_4 in the reactor.

3 Results and Discussion

3.1 Characterization

Table 1 shows the main physic-chemical properties of the prepared Ni/CeO_2 catalysts. The Ni/CeO_2-nrs catalyst exhibited the highest surface area followed by the Ni/CeO_2-nps and Ni/CeO_2-ncs catalysts. As noted, a large surface area is conducive to the dispersion of active metals and the exposure of active sites [22].

TEM and EDX images of CeO_2 supports with different morphologies or the corresponding Ni/CeO_2 catalysts are presented in Fig. 1. Figure 1-A1 displays the CeO_2 nanorods and the average length of these rods is about 100–200 nm while the diameter is approximate 15–20 nm. The interplanar spacing of 0.19 and 0.27 nm on the HRTEM images of an isolated nanosheet have lattice fringe directions attributed

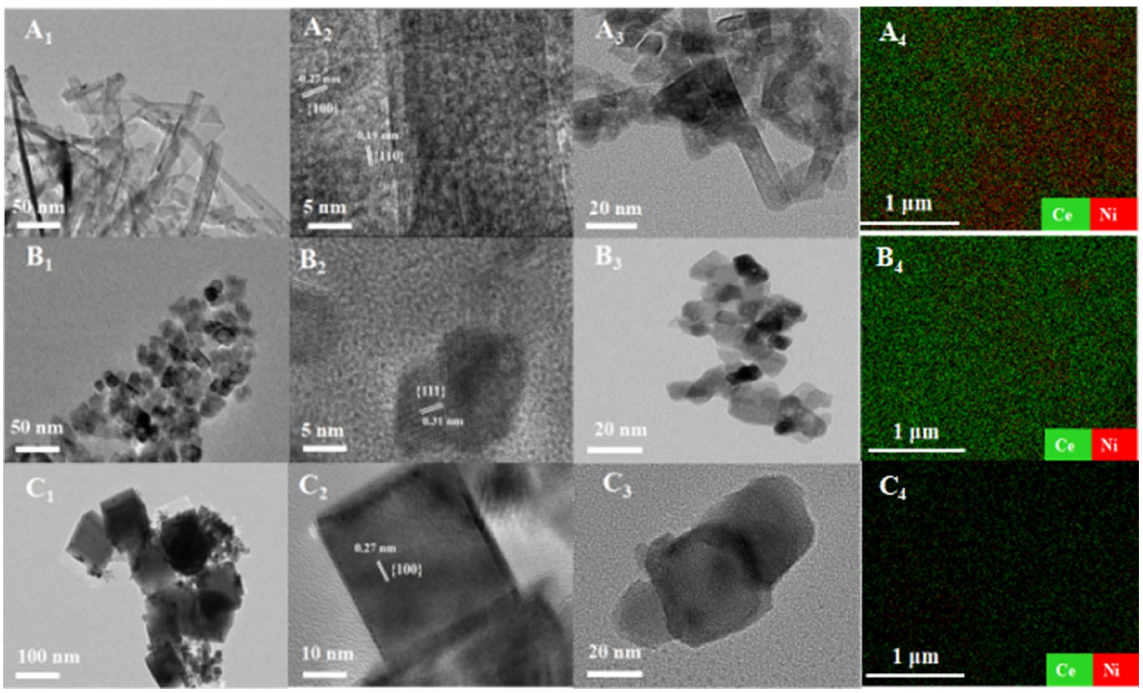

Fig. 1 TEM and EDX images of CeO_2 supports with different morphologies or the corresponding Ni/CeO_2 catalysts

to {110} and {100}, as observed in Fig. 1-A2. In Fig. 1-B1, the CeO_2-nps consists of nanoparticles with average diameter of about 9.5 nm. The corresponding HRTEM image (Fig. 1-B2) shows that the interplanar spacing of 0.31 nm has a lattice fringe direction attributed to {111} planes. For the CeO_2 nanocubes (CeO_2-ncs) shown in Fig. 1-C1, the particle size ranges from 15 to 100 nm, and the lattice structure is discerned with spacing of 0.27 nm (Fig. 1-C2) close to the lattice spacing measured for {100} planes. The TEM images of nickel-loading CeO_2 catalysts shown in Fig. 1-A3, B3, and C3 indicate that there is no significant change in the morphology of CeO_2 following the nickle loading. Furthermore, EDX-mapping in Fig. 1 (Fig. 1-A4, B4, and C4 for CeO_2-nrs CeO_2-nps and CeO_2-ncs, respectively) could elucidate that most of Ni particles were incorporated in the CeO_2 nanostructure in these three catalysts. The Ni/CeO_2-nrs catalysts displayed the best Ni dispersion, and the elements Ni and Ce were uniformly distributed in the catalyst.

The XRD patterns of the CeO_2 supports (Fig. 2a), and the calcined (Fig. 2b) and reduced (Fig. 2c) Ni/CeO_2 catalysts are shown in Fig. 2. The peaks appeared at 28.5°, 33.1°, 47.5°, 56.3°, 59.1°, and 69.4° in Fig. 2a are attributed to the {111}, {200}, {220}, {311}, {222} and {400} planes of CeO_2. No diffraction peaks of hexagonal crystal forms such as $Ce(OH)_3$ and $Ce(OH)CO_3$ are found, indicating the CeO_2 supports exhibit good crystal purity [23]. The XRD patterns of the calcined Ni/CeO_2 catalysts in Fig. 2b display additional diffraction peaks at 37.2°, 43.3° and 62.9°, corresponding to the {111}, {200}, and {220} planes of NiO, respectively. After reduced under a stream of 10 vol.% H_2/N_2 (50 mL min^{-1}) at 600 °C for 4 h, the diffraction peaks of NiO in the catalysts disappear completely, while Ni peaks present at 44.6°, 51.9° and 76.5° corresponding to the {111}, {200} and {220} planes, respectively as shown in Fig. 2c. The crystal sizes of the metallic Ni calculated using the Scherrer-equation for the {200} plane at 51.9° are 8.2, 29.6, and 31.4 nm for Ni/CeO_2-nrs, Ni/CeO_2-nps and Ni/CeO_2-ncs, respectively.

The interaction between NiO and support in the catalysts was analyzed by H_2-TPR (Fig. 3). The Ni/CeO_2 catalysts mainly exhibit three reduction peaks. The peaks at 247–255 °C and 347–355 °C are attributed to the reduction of NiO. The former corresponds to the reduction of the bulk NiO that has no or weak interaction with CeO_2, while the latter represents the reduction of the NiO that has strong interaction with support. In addition, the peak at 831–858 °C is attributed to the reduction of CeO_2 [24]. The H_2-TPR profiles show that the NiO particles in all Ni/CeO_2 catalysts could be completely reduced to metallic nickel after reduced at 600 °C for 4 h in accordance with the result of XRD patterns in Fig. 2c.

The Ni/CeO_2 catalysts were characterized by H_2-TPD to explore their H_2 adsorption capacity, and the results are

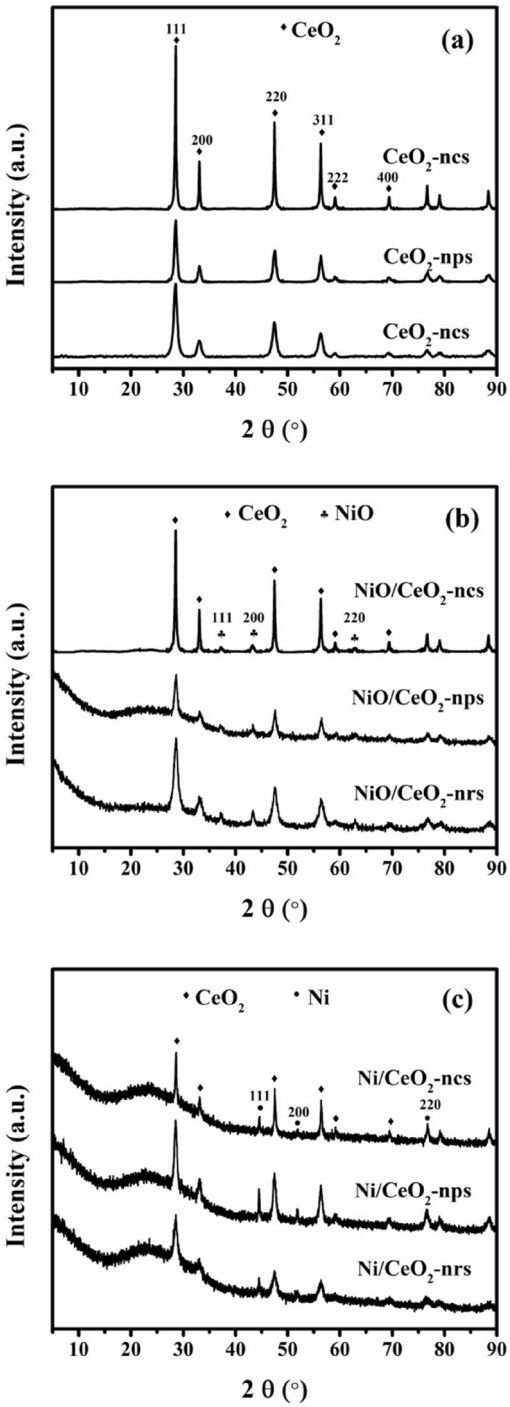

Fig. 2 XRD profiles of CeO_2 supports with different morphologies (**a**) and calcined (**b**) and reduced (**c**) Ni/CeO_2 catalysts

shown in Fig. 4. The first peak before 400 °C belongs to the weakly active sites of the metal on the catalyst surface. The second peak after 400 °C is attributed to the active sites strongly chemisorbed on the surface. It can be found that the H_2 desorption peaks of the three catalysts are mainly before 300 °C, and the H_2 desorption area of Ni/CeO_2-nrs is

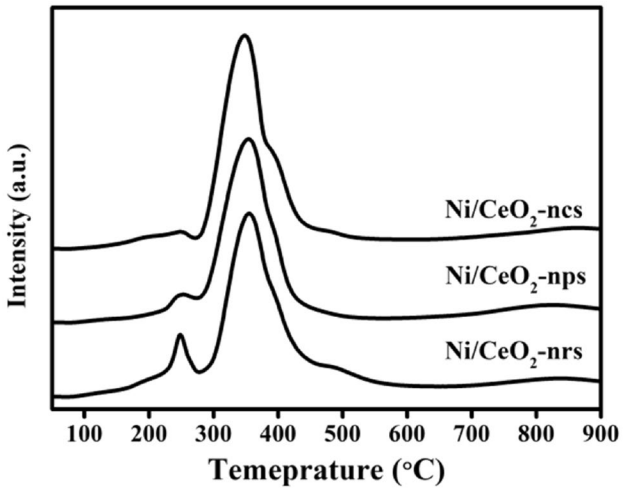

Fig. 3 H_2-TPR profiles of Ni/CeO_2 catalysts

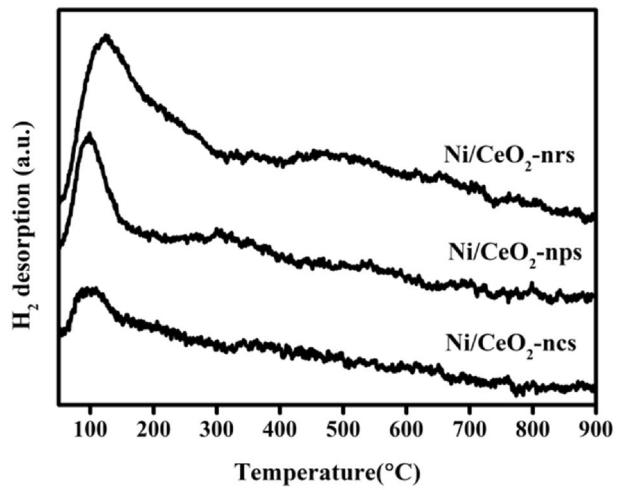

Fig. 4 H_2-TPD profiles of Ni/CeO_2 catalysts

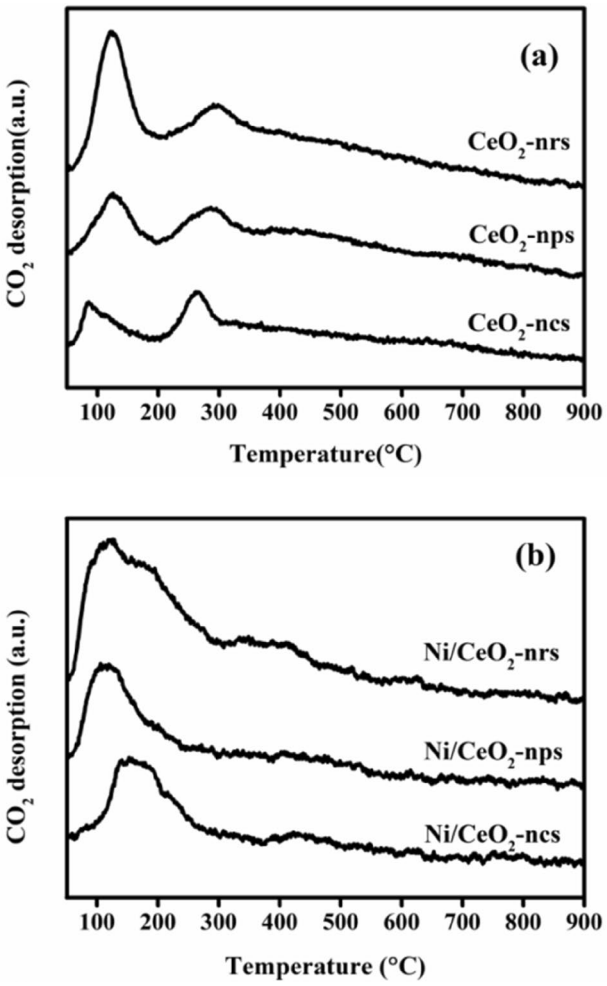

Fig. 5 CO_2-TPD profiles of CeO_2 supports with different morphologies (**a**) and Ni/CeO_2 catalysts (**b**)

significantly higher than other two catalysts, which indicate that its H_2 adsorption capacity is the strongest. The nickel dispersion and average nickel diameter calculated from the H_2-TPD profiles are displayed in Table 1.The dispersion of active sites in the Ni-based catalysts follows an order of Ni/CeO_2-nrs > Ni/CeO_2-nps > Ni/CeO_2-ncs.

The CO_2 adsorption capacity plays an important role in maintaining the catalytic activity for CO_2 methanation. Therefore, CO_2-TPD of the CeO_2 supports and Ni/CeO_2 catalysts were carried out and the results are shown in Fig. 5. For CeO_2 supports, the low-temperature desorption peak at 85–130 °C is attributed to the CO_2 interacted with the weak basic sites on the surface (Fig. 5a). The broad adsorption peak between 260 and 294 °C is considered to be related to the moderate basic sites on the CeO_2 [25–27]. The area of the peak attributed to the weak basic sites in CeO_2-nrs is the largest indicating the CeO_2 nanorods support is more conducive to CO_2 adsorption at low temperatures. As shown in Fig. 5b, the desorption peaks corresponding to the weak and moderate basic sites overlaps between 80 and 300 °C after nickel loading. In addition, the Ni/CeO_2-nrs catalyst exhibits the largest area of CO_2 desorption peaks. The CO_2 adsorptions are calculated to be 60, 25 and 19 μmol g_{cat}^{-1} for Ni/CeO_2-nrs, Ni/CeO_2-nps, and Ni/CeO_2-ncs, respectively.

The electronic properties of the metal oxide and the adsorbed species on the catalysts also play an important role in the hydrogen and carbon dioxide activation. Figure 6 displays XPS spectra for the reduced Ni/CeO_2 catalysts, revealing peaks assigned to O 1s, Ni 2p, and Ce 3d. Two obvious surface oxygen peaks are observed in the O 1s spectrum, where the binding energy at 529.1 ± 0.1 eV is assigned to lattice oxygen species (O_L), and the peak at 530.9 ± 0.2 eV is characteristic of O^{2-} in oxygen deficient regions (O_V). The ratio of O_V/O_L can be used to represent the concentration

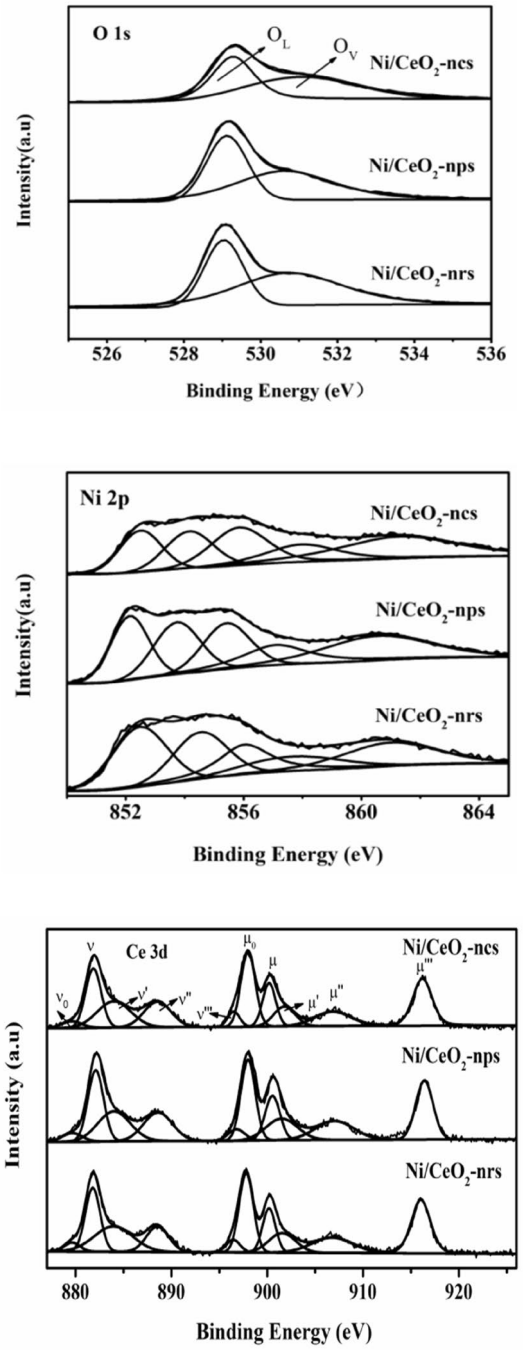

Fig. 6 X-ray photoelectron spetra of the reduced Ni/CeO_2 catalysts

of surface oxygen vacancies on CeO_2 surface [19]. Table 2 shows that the ratio of O_V/O_L decreases in an order of Ni/CeO_2-nrs > Ni/CeO_2-nps > Ni/CeO_2-ncs. It has been reported that CO_2 molecules could be reduced by the oxygen deficient regions to form CO species to realize CO_2 activation ($CeO_{2-\delta} + CO_2 \rightarrow CeO_2 + CO$). [21].

Peaks for different oxidation states of Ni in the reduced Ni/CeO_2 catalysts were assigned based on Gaussian fitting and literatures [28, 29]. The split peak at 852.5 eV in the Ni 2p spectrum corresponds to metallic Ni, while the peak observed at 854.5, 856.1 and 857.8 eV corresponds to the binding energy of NiO which were strongly bonded with CeO_2, and the accompanying peak appears at 861.1 eV. Table 2 shows that the ratio of Ni^0/Ni^{2+} also follows an order of Ni/CeO_2-nrs > Ni/CeO_2-nps > Ni/CeO_2-ncs. Kim et al. found that the content of Ni^0 in the Ni/CeO_2 catalyst correlates with the surface electron states of Ce, and it increased with the Ce^{3+} rising [30].

Table 2 Calculation results of XPS peaks for different elements

Catalyst	O_V/O_L	Ni^0/Ni^{2+}	Ce^{3+}/Ce^{4+}
Ni/CeO_2-nrs	1.59	0.37	0.7
Ni/CeO_2-nps	1.26	0.26	0.67
Ni/CeO_2-ncs	1.14	0.19	0.65

A complex peak pattern is shown and ten peaks are fitted for the Ce 3d spectrum. The v_0 (879.6 eV), ν (881.8 eV), v′ (884.0 eV), v″ (888.6 eV), and v‴ (896.5 eV) labeled peaks in the figure refer to the spin–orbit coupling $3d_{5/2}$, while the μ_0 (898.0 eV), μ (900.2 eV), μ′ (901.8 eV), μ″ (906.9 eV), and μ‴ (916.2 eV) peaks are associated with $3d_{3/2}$. The v‴, μ‴, v″, μ″, ν, and μ peaks are characteristics of Ce^{4+} corresponding to the Ce $3d^94f^0$ O $2p^6$, Ce $3d^94f^1$ O $2p^5$, and Ce $3d^94f^2$ O $2p^4$ electrons, respectively. Meanwhile, the v′, μ′, v_0 and μ_0 peaks are characteristics of Ce^{3+} corresponding to the Ce $3d^94f^1$ O $2p^6$ and Ce $3d^94f^2$ O $2p^5$ electrons, respectively [31]. The ratio of the cumulative intensities of all peaks assigned to Ce^{3+} and the cumulative intensities of all peaks assigned to Ce^{4+} is a measure for the Ce^{3+}/Ce^{4+} atomic ratio, as shown in Table 2. A higher ratio of Ce^{3+}/Ce^{4+} indicates the presence of more oxygen vacancies, since the presence of oxygen vacancies maintains the electronic balance between Ce^{3+} and Ce^{4+} (Eq. 5) [27]. Some previous studies have shown that the presence of oxygen vacancies induces the production of O^{2-} or OH groups on the surface due to adsorption of water and the CO_2 adsorption capacity of a catalyst is related to the –OH and O^{2-} species present on the support [32, 33]. Therefore, from Table 2 the Ni/CeO_2-nrs catalyst contains a greater concentration of oxygen vacancies and Ni^0, thereby rendering its CO_2 adsorption capacity superior to those of the other two catalysts.

$$4Ce^{4+} + O^{2-} \rightarrow 4Ce^{4+} + \frac{2e^-}{\delta} + 0.5O_2 \rightarrow 2Ce^{4+} + 2Ce^{3+} + \delta + 0.5O_2 \quad (5)$$

3.2 Catalytic Activity

The CO_2 conversion and CH_4 selectivity for CO_2 methanation over the Ni/CeO_2 catalysts at different temperatures are presented in Fig. 7, whereby the thermodynamic

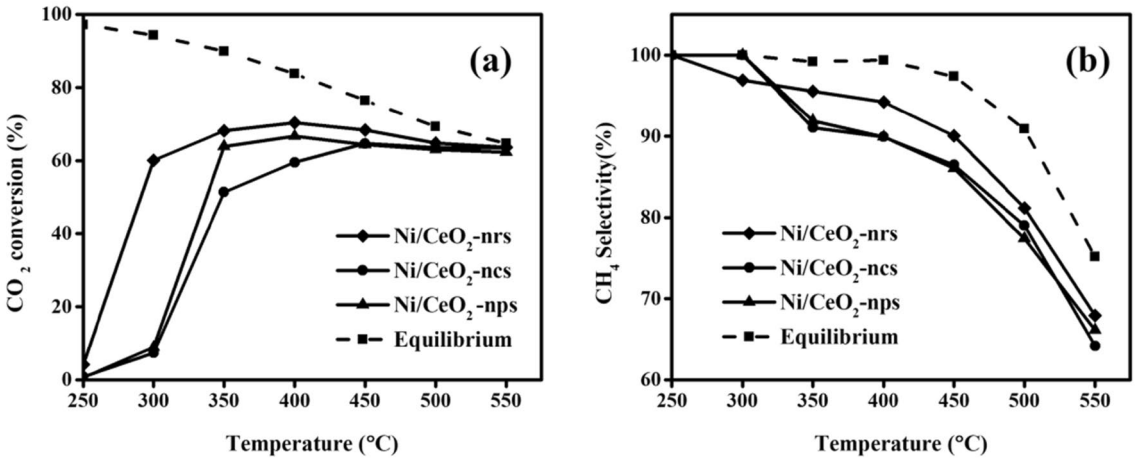

Fig. 7 CO_2 conversion (**a**) and CH_4 selectivity (**b**) for CO_2 methanation over Ni/CeO_2 catalysts

equilibrium values were calculated by minimizing the Gibbs free energy method. As shown in Fig. 7a, the CO_2 conversion increases rapidly as raising the temperature from 250 to 400 °C, and then decreases gradually from 400 to 550 °C for all the three Ni/CeO_2 catalysts. However, the CH_4 selectivity decreases as increasing the temperature from 250 to 550 °C (Fig. 7b), because the water–gas shift reaction takes place at higher temperatures, which converts CO_2 into CO instead of CH_4 [34]. Meanwhile, as temperatures lower than 450 °C, the CO_2 conversion follows an order of Ni/CeO_2-nrs > Ni/CeO_2-nps > Ni/CeO_2-ncs. Especially, the CO_2 conversion and CH_4 selectivity at 300 °C are 60.1 and 96.9% for Ni/CeO_2-nrs, respectively, while the CO_2 conversions for the other two catalysts are both less than 10%. In addition, it is obvious that at lower temperatures (250–450 °C), the CO_2 conversion is much lower than the equilibrium data which reveals that the CO_2 methanation is subject to kinetic control.

The promotion effect of oxygen vacancy on the catalytic activity of Ni-CeO_2 catalyst in the CO_2 methanation is also evaluated by the turnover frequency (TOF) values. To ignore the potential effect of mass and heat transfer, the TOF values was calculated at 250 °C (where CO_2 conversion was less than 15%). The TOF of samples were calculated as moles of CH_4 produced per mole of surface Ni atoms per second according to the methods reported [16, 35, 36]. From Fig. 8, it is observed that TOFs follow an order of Ni/CeO_2-nrs (0.111 s^{-1}) > Ni/CeO_2-nps (0.078 s^{-1}) > Ni/CeO_2-ncs (0.066 s^{-1}), confirming the CO_2 conversion and CH_4 selectivity in Fig. 7. The TOF values increase linearly with the concentration of oxygen vacancy in the catalyst, indicating the oxygen vacancy can improve the CO_2 adsorption and activation, and then result in the improvement of the intrinsic activity of the catalyst.

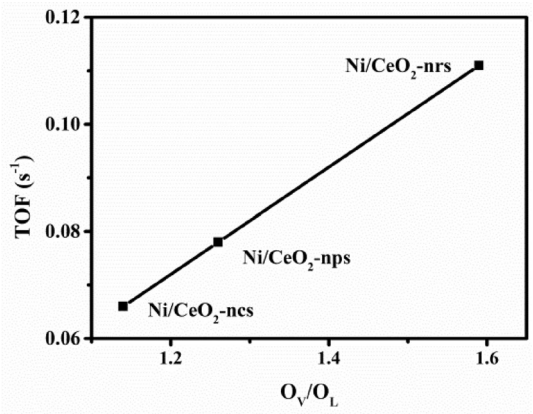

Fig. 8 The effect of surface oxygen vacancy (O_V/O_L) on turnover frequency (TOF) at 250 °C

3.3 Discussion

According to the results above, the Ni/CeO_2-nrs catalyst exhibited well metal dispersion and CO_2 adsorption capacity, thereby resulting in a significantly high CO_2 conversion during CO_2 methanation compared to the other two catalysts. Previous studies have shown [21] that the surface area of the support played an important role in the dispersion of active metals. However, the structure parameters affecting the CO_2 adsorption capacity require further discussion.

The adsorption capacity of Ni-based catalysts toward CO_2 is mainly related to their basic sites [37–39], whereby the type and concentration of basic sites are influenced by the oxygen vacancy present in the support [16]. Thus, the quantitative relationship between the oxygen vacancy and the specific surface area is investigated and the result is shown in Fig. 9. As indicated, the oxygen vacancy concentration and the Brauner–Emmett–Teller (BET) surface area are

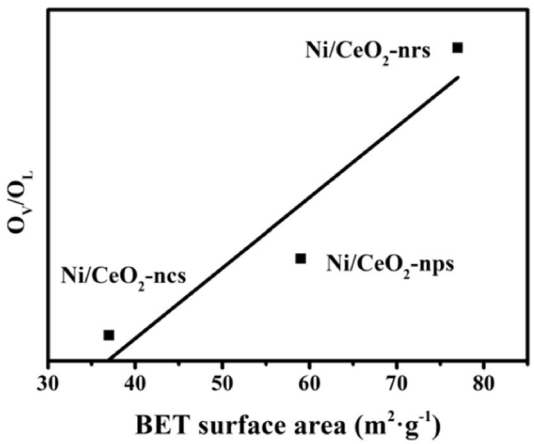

Fig. 9 The relationship between BET surface area and concentration of oxygen vacancy (O_V/O_L) in Ni/CeO_2 catalysts

positively correlated, and the Ni/CeO_2-nrs catalyst seems possessing the largest surface area and then the largest oxygen vacancy concentration.

From Table 1, the surface area of the Ni/CeO_2-nrs catalyst is approximately twice that of the Ni/CeO_2-ncs catalyst. Therefore, an additional test was carried out to double the quality of Ni/CeO_2-ncs for the CO_2 methanation whereas with unchanged gas residence time with catalyst bed, and then the CO_2 conversion and CH_4 selectivity were compared with the performance of Ni/CeO_2-nrs. As shown in Fig. 10, the CO_2 conversion and CH_4 selectivity over the Ni/CeO_2-ncs catalyst are improved significantly and approach to that over Ni/CeO_2-nrs in the temperature range of 250–550 °C. This result indicates that CO_2 adsorption and activation capacity is rate-determining step for CO_2 methanation, especially at low temperatures, because doubling the quantity of the Ni/CeO_2-ncs catalyst could increase the total oxygen vacancy content for CO_2 adsorption and activation, thereby further improve the CO_2 conversion and CH_4 selectivity.

4 Conclusions

Three Ni/CeO_2 catalysts with different morphologies were prepared and the catalytic activity for CO_2 methanation was evaluated. It was found that the Ni/CeO_2 nanorods catalyst exhibited the highest CO_2 conversion, especially at temperatures lower than 400 °C. At 300 °C, the CO_2 conversion reached 60% compared to 10% achieved over Ni/CeO_2 nanopolyhedrons and Ni/CeO_2 nanocubes. However, catalytic activity of CO_2 methanation over doubled quantity of Ni/CeO_2 nanocubes catalyst approximately approached to that over Ni/CeO_2 nanorods catalyst at the same gas residence time. Combining the characterizations, it could be concluded that the oxygen vacancy in the Ni/CeO_2 catalyst, which is related with its morphology and surface area is conducive to the low-temperature adsorption of CO_2, and then the catalytic activity for CO_2 methanation.

Acknowledgements This work was supported by the Fund of International Science and Technology Cooperation Program of China (2019YFC1906802).

Declaration

Competing interest There have no competing interest.

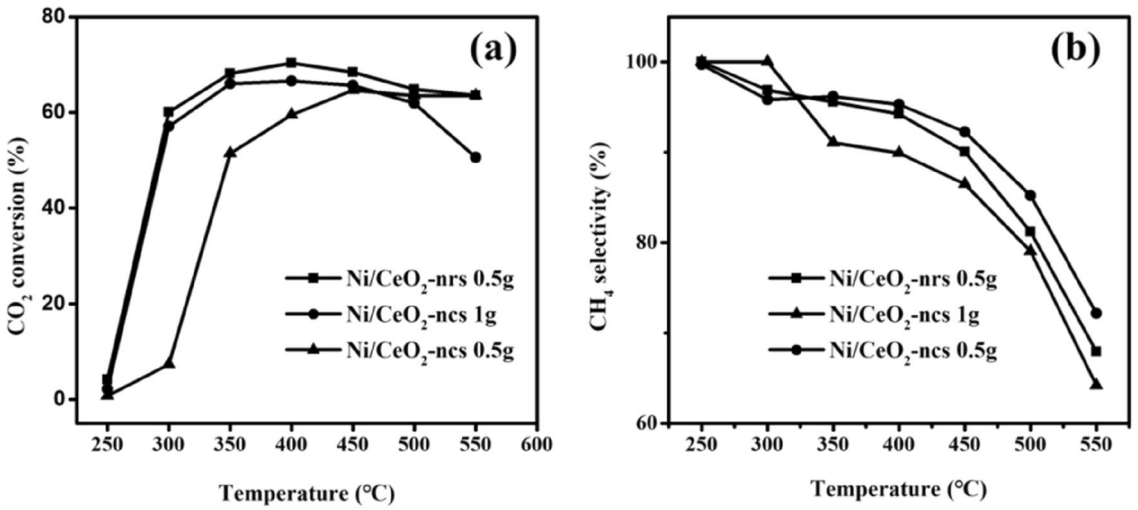

Fig. 10 CO_2 conversion (**a**) and CH_4 selectivity (**b**) for CO_2 methanation over Ni/CeO_2-ncs catalyst with different catalyst amount

References

1. Zhen W, Gao F, Tian B et al (2017) Enhancing activity for carbon dioxide methanation by encapsulating (111) facet Ni particle in metal–organic frameworks at low temperature. J Catal 348:200–211. https://doi.org/10.1016/j.jcat.2017.02.031
2. Ma Y, Liu J, Chu M et al (2020) Cooperation between active metal and basic support in Ni-based catalyst for low-temperature CO_2 methanation. Catal Lett 150:1418–1426. https://doi.org/10.1007/s10562-019-03033-w
3. Hu L, Urakawa A (2018) Continuous CO_2 capture and reduction in one process: CO_2 methanation over unpromoted and promoted Ni/ZrO_2. J CO2 Util 25:323–329. https://doi.org/10.1016/j.jcou.2018.03.013
4. Younas M, Loong KL, Bashir MJK et al (2016) Recent advancements, fundamental challenges, and opportunities in catalytic methanation of CO_2. Energ Fuel 30:8815–8831. https://doi.org/10.1021/acs.energyfuels.6b01723
5. Li W, Zhang A, Jiang X et al (2017) Low temperature CO_2 methanation: ZIF-67-derived Co-based porous carbon catalysts with controlled crystal morphology and size. Acs Sustain Chem Eng 5:7824–7831. https://doi.org/10.1021/acssuschemeng.7b01306
6. Danaci S, Protasova L, Lefevere J et al (2016) Efficient CO_2 methanation over Ni/Al_2O_3 coated structured catalysts. Catal Today 273:234–243. https://doi.org/10.1016/j.cattod.2016.04.019
7. Muroyama H, Tsuda Y, Asakoshi T et al (2016) Carbon dioxide methanation over Ni catalysts supported on various metal oxides. J Catal 343:178–184. https://doi.org/10.1016/j.jcat.2016.07.018
8. Ma S, Tan Y, Han Y (2011) Methanation of syngas over coral reef-like Ni/Al_2O_3 catalysts. J Nat Gas Chem 20:435–440. https://doi.org/10.1016/S1003-9953(10)60192-2
9. Takenaka S, Shimizu T, Otsuka K (2004) Complete removal of carbon monoxide in hydrogen-rich gas stream through methanation over supported metal catalysts. Int J Hydrogen Energy 29:1065–1073. https://doi.org/10.1016/j.ijhydene.2003.10.009
10. Zyryanova MM, Snytnikov PV, Gulyaev RV et al (2014) Performance of Ni/CeO_2 catalysts for selective CO methanation in hydrogen-rich gas. Chem Eng J 238:189–197. https://doi.org/10.1016/j.cej.2013.07.034
11. Sun J, Wang Y, Zou H et al (2019) Ni catalysts supported on nanosheet and nanoplate γ-Al_2O_3 for carbon dioxide methanation. J Energy Chem 29:3–7. https://doi.org/10.1016/j.jechem.2017.09.029
12. Tada S, Shimizu T, Kameyama H et al (2012) Ni/CeO_2 catalysts with high CO_2 methanation activity and high CH_4 selectivity at low temperatures. Int J Hydrogen Energy 37:5527–5531. https://doi.org/10.1016/j.ijhydene.2011.12.122
13. Huang J, Li X, Wang X et al (2019) New insights into CO_2 methanation mechanisms on Ni/MgO catalysts by DFT calculations: elucidating Ni and MgO roles and support effects. J CO2 Util 33:55–63. https://doi.org/10.1016/j.jcou.2019.04.022
14. Frontera P, Macario A, Ferraro M et al (2017) Supported catalysts for CO_2 methanation: a review. Catalyst 7:59. https://doi.org/10.3390/catal7020059
15. Pan Q, Peng J, Sun T et al (2014) Insight into the reaction route of CO_2 methanation: promotion effect of medium basic sites. Catal Commun 45:74–78. https://doi.org/10.1016/j.catcom.2013.10.034
16. Jia X, Zhang X, Rui N et al (2019) Structural effect of Ni/ZrO_2 catalyst on CO_2 methanation with enhanced activity. Appl Catal B Environ 244:159–169. https://doi.org/10.1016/j.apcatb.2018.11.024
17. Wang F, He S, Chen H et al (2016) Active site-dependent reaction mechanism over Ru/CeO_2 catalyst toward CO_2 methanation. J Am Chem Soc 138:6298–6305. https://doi.org/10.1021/jacs.6b02762
18. Mai H, Sun L, Zhang Y et al (2015) Shape-selective synthesis and oxygen storage behavior of ceria nanopolyhedra, nanorods, and nanocubes. J Phys Chem B 109:24380–24385. https://doi.org/10.1021/jp055584b
19. Sakpal T, Lefferts L (2018) Structure-dependent activity of CeO_2 supported Ru catalysts for CO_2 methanation. J Catal 367:171–180. https://doi.org/10.1016/j.jcat.2018.08.027
20. Varvoutis G, Lykaki M, Konsolakis M et al (2020) Remarkable efficiency of Ni supported on hydrothermally synthesized CeO_2 nanorods for low-temperature CO_2 hydrogenation to methane. Catal Commun 142:106036–106040. https://doi.org/10.1016/j.catcom.2020.106036
21. Zhou G, Liu H, Cui K et al (2016) Role of surface Ni and Ce species of Ni/CeO_2 catalyst in CO_2 methanation. Appl Surf Sci 383:248–252. https://doi.org/10.1016/j.apsusc.2016.04.180
22. Zhu P, Chen Q, Yoneyama Y (2014) Nanoparticle modified Ni-based bimodal pore catalysts for enhanced CO_2 methanation. RSC Adv 4:64617–64624. https://doi.org/10.1039/C4RA12861C
23. Li L, Jiang B, Tang D et al (2018) Hydrogen production from chemical looping reforming of ethanol using Ni/CeO_2 nanorod oxygen carrier. Catalysts 8:257. https://doi.org/10.3390/catal8070257
24. Damyanova S, Bueno JMC (2003) Effect of CeO_2 loading on the surface and catalytic behaviors of CeO_2-Al_2O_3-supported Pt catalysts. Appl Catal A Gen 253:135–150. https://doi.org/10.1016/S0926-860X(03)00500-3
25. Moghaddam SV, Rezaei M, Meshkani F et al (2018) Carbon dioxide methanation over Ni-M/Al_2O_3 (M: Fe, CO, Zr, La and Cu) catalysts synthesized using the one-pot sol–gel synthesis method. Int J Hydrogen Energy 43:16522–16533. https://doi.org/10.1016/j.ijhydene.2018.07.013
26. Yu Y, Chan YM, Bian Z et al (2018) Enhanced performance and selectivity of CO_2 methanation over g-C_3N_4 assisted synthesis of Ni-CeO_2 catalyst: kinetics and DRIFTS studies. Int J Hydrogen Energy 43:15191–15204. https://doi.org/10.1016/j.ijhydene.2018.06.090
27. Pino L, Vita A, Cipitì F et al (2011) Hydrogen production by methane tri-reforming process over Ni-ceria catalysts: effect of La-doping. Appl Catal B Environ 104:64–73. https://doi.org/10.1016/j.apcatb.2011.02.027
28. Li M, Veen AC (2018) Tuning the catalytic performance of Ni-catalysed dry reforming of methane and carbon deposition via Ni-CeO_2-x interaction. Appl Catal B Environ 237:641–648. https://doi.org/10.1016/j.apcatb.2018.06.032
29. Chen X, Li M, Guan J et al (2012) Nickel-silicon intermetallics with enhanced selectivity in hydrogenation reactions of cinnamaldehyde and phenylacetylene. Ind Eng Chem Res 51:3604–3611. https://doi.org/10.1021/ie202227j
30. Kim MJ, Youn J, Kim HJ et al (2020) Effect of surface properties controlled by Ce addition on CO_2 methanation over Ni/Ce/Al_2O_3 catalyst. Int J Hydrogen Energy 45:24595–24603. https://doi.org/10.1016/j.ijhydene.2020.06.144
31. Bêche E, Charvin P, Perarnau D et al (2008) Ce 3d XPS investigation of cerium oxides and mixed cerium oxide ($Ce_xTi_yO_z$). Surf Interface Anal 40:264–267. https://doi.org/10.1002/sia.2686
32. Souza MMVM, Aranda DAG, Schmal M (2001) Reforming of methane with carbon dioxide over Pt/ZrO_2/Al_2O_3 catalysts. J Catal 204:498–511. https://doi.org/10.1006/jcat.2001.3398
33. Drorouilly KJM, Averseng F et al (2013) Role of oxygen vacancies in the basicity of ZnO: from the model methylbutynol conversion to the ethanol transformation application. Appl Catal A Gen 453:121–129. https://doi.org/10.1016/j.apcata.2012.11.045
34. Stangeland K, Kalai DY, Li H et al (2018) Active and stable Ni based catalysts and processes for biogas upgrading: the effect of temperature and initial methane concentration on CO_2

methanation. Appl Energy 227:206–212. https://doi.org/10.1016/j.apenergy.2017.08.080
35. Chen H, Mu Y, Shao Y et al (2019) Coupling non-thermal plasma with Ni catalysts supported on BETA zeolite for catalytic CO_2 methanation. Catal Sci Technol 9:4135. https://doi.org/10.1039/C9CY00590K
36. Li LJ, Yi WJ, Liu TW et al (2017) Hydrogenation of 3-hydroxypropanal into 1,3-propanediol over bimetallic Ru–Ni catalyst. RSC Adv 7:32027–32037. https://doi.org/10.1039/C7RA01184A
37. Song F, Zhong Q, Yu Y et al (2017) Obtaining well-dispersed Ni/Al_2O_3 catalyst for CO_2 methanation with a microwave-assisted method. Int J Hydrogen Energy 42:4174–4183. https://doi.org/10.1016/j.ijhydene.2016.10.141
38. Quindimil A, De-La-Torre U, Pereda-Ayo B et al (2018) Ni catalysts with La as promoter supported over Y- and BETA-zeolites for CO_2 methanation. Appl Catal B Environ 238:393–403. https://doi.org/10.1016/j.apcatb.2018.07.034
39. Park JN, McFarland EW (2009) A highly dispersed Pd-Mg/SiO_2 catalyst active for methanation of CO_2. J Catal 266:92–97. https://doi.org/10.1016/j.jcat.2009.05.018